Article

Thermal Assessment of a Ventilated Double Skin Façade Component with a Set of Air Filtering Photocatalytic Slats in the Cavity

Oriol Roig [1,*], Eva Cuerva [2,3], Cristina Pardal [1], Alfredo Guardo [4], Antonio Isalgue [5] and Judit Lopez-Besora [1]

1   Tecnologia de l'Arquitectura, ETSAB-UPC Edifici Segarra, Av. Diagonal, 649, 08028 Barcelona, Spain
2   Department of Project and Construction Engineering, ETSEIB-UPC, Av. Diagonal, 647, 08028 Barcelona, Spain
3   Group of Construction Research and Innovation (GRIC), C/Colom 11, Edifici TR5, 08222 Terrassa, Spain
4   Centre de Diagnòstic Industrial i Fluidodinàmica (UPC CDIF)/Fluid Mechanics Department,
    Escola d'Enginyeria de Barcelona Est (EEBE), Edifici A. C/Eduard Maristany, 16, 08019 Barcelona, Spain
5   Departament de Física, UPC, Edifici NT1, Pla De Palau, 18, 08003 Barcelona, Spain
*   Correspondence: oriol.roig.mayoral@upc.edu

Abstract: Indoor air quality is a crucial factor when evaluating habitability, especially in developed countries, where people spend most of their time indoors. This paper presents a novel double skin façade (DSF) system that combines physical and photocatalytic filtering strategies. The air purification system is made up of fixed slats that are both solar protection and air purification system. The objective of this work is to determine the thermal behaviour of the proposed system, so that its suitability for use in various environments may be assessed. This was carried out using a physical 1:1 scale model and a computational fluid dynamics (CFD) model. The maximum temperature inside the scale model cavity was 17–20 °C higher than outdoor air. Additionally, it was discovered that the airflow through the DSF would require forced ventilation. To determine the emissivity values of the photocatalytic coating, additional experimental measurements were made. The CFD model was tested for summer and winter conditions in Barcelona, Chicago, and Vancouver. The average increase in the intake air temperature was around 14.5 °C in winter and 12 °C in summer, finding that the system has its main use potential in temperate or cold areas with many hours of solar radiation.

Keywords: indoor air quality; integrated façade systems; active filtering façade; façade thermal performance; computational fluid dynamics

1. Introduction

Indoor air quality in buildings is an issue of growing importance, which unfortunately has become more evident due to the pandemic caused by SARS-CoV-2. However, apart from this exceptional situation that we are currently experiencing, some studies estimate that, on average, people in developed countries spend about 90% of their time indoors [1]. This makes it vital to boost improvements in indoor conditions, which become essential for ensuring a healthy environment for building users [2].

The concept of "habitability", as defined by the United Nations [3], considers several parameters and conditions that buildings must comply with in order to guarantee the safety, comfort, and security of their inhabitants. Ventilation and indoor air quality (IAQ) are of central importance [4], as they can keep temperature, humidity, and CO_2, as well as air pollutants/contaminants, within the ranges defined by building regulations and certifications [5]. They also reduce the possibility of inner wall condensation, which can be responsible for wall deterioration, mould growth, and unhealthy living conditions. In this respect, there are studies that claim that about 84 million Europeans live in damp or wet houses, which can increase their risk of developing asthma, influenza, bronchitis, or migraines by up to 40% [6].

When dealing with building ventilation, one possibility is to use passive systems that do not consume energy. Natural ventilation, performed through operable windows that can be controlled by users, guarantee the intake of fresh air, as well as the possibility for the user to interact with the building, improving their wellbeing [7–10]. Other systems that could be implemented in buildings in order to improve ventilation rates include, for example, double skin strategies, atriums, different types of façade, and rooftop openings, as well as mechanical ventilation systems [11,12]. Among these systems, ventilated double skin façades (VDSF) are noteworthy. This type of façade basically consists of two layers (usually fully glazed) separated by an air cavity (ranging from a few centimetres to up to 2 m in width); this cavity can be ventilated (naturally or mechanically) or not [13,14].

VDSF have multiple advantages when compared to a conventional curtain wall (or single skin façade). Among others, they improve the acoustic performance of the façade, increase the thermal insulation of the building envelope, and allow the user to interact with the façade (as openings in the inner layer may also be operable). They make it possible to reuse the exhaust air of the building, directly or with heat exchangers, as preheated air for the air conditioning units leading to reduced energy consumption. They also enable solar protection to be installed within the cavity, thereby extending its lifespan [14–19]. However, depending on the building location, the naturally ventilated VDSF can lead to overheating inside the building. This occurs mainly under summer conditions in the Mediterranean or other mild or warm climates [20–22]. Under these circumstances, solar protection, as well as mechanical ventilation of the façade cavity, may be needed in order to reduce the solar radiation entering the building and to maximize heat extraction through the façade [23–25].

Nevertheless, despite the possibilities of VDSF for natural ventilation, when exterior air conditions are inadequate, outdoor air intake can become a problem. Air pollution, caused by volatile organic compounds (VOCs), suspended particles (dust, pollen, spores), or chemical compounds (NO_x, O_3, CO, SO_2), is directly connected to health conditions such as allergies and asthma, among others [26,27]. Thus, in a context where periods of intense air pollution become increasingly common in our cities, measures are needed to ensure that the air entering buildings is free of contaminants.

Natural ventilation systems usually operate with no external air filtration. On the other hand, mechanical ventilation systems incorporate air treatment units (AHUs) that, among other functions, include physical filtering stages. These filters reduce or eliminate suspended particles, but they do not eliminate harmful chemical compounds present in the outdoor air. Chemical reactions are required in order to remove small-sized particles and chemicals that are difficult to retain using physical filters [28].

Chemical reactions for purifying air can be classified into two groups: organic, using photosynthesis or photobioreaction (e.g., by means of green roofs or green façades); and inorganic, using photocatalysis [29]. Photocatalytic systems comprise a chemical compound (such as titanium dioxide, TiO_2) that separates out polluting elements when in contact with the oxygen present in the air and with UV solar radiation, which is needed to activate the chemical process [30,31]. When used as an air-cleaning system in buildings, the photocatalytic element is applied as a coating to an exposed surface [32,33].

The tendency in the development of façade construction systems points towards prefabrication and standardization. Integrated façade components combinate different industries and materials in a single construction system, while modern technologies allow complex designs of façade components [34,35], which fulfil all the functional requirements of the enclosure [36,37].

In this paper, an innovative façade system combining both physical and photocatalytic filtering strategies is presented. The façade consists of a fully glazed, ventilated double skin façade component. The cavity contains a set of fixed slats that constitute the air purification system, with both physical filtering and photocatalytic elements. The slats also provide solar protection to the building interior, while allowing the view to the outside. However, given that the façade surfaces are glazed to ensure the photocatalytic reaction, overheating problems can occur in some situations [38]. This potential problem makes

it necessary to determine the thermal performance of the system in order to evaluate its application in different outdoor environmental conditions. In certain contexts, and with adequate configuration, this system can provide valuable heat gains during cold periods by preheating the intake ventilation air [38,39]. Thus, the main goal of this research lies in determining the thermal character of the proposed façade system.

This thermal analysis was performed using a mixed approach. A 1:1 scale model of a part-section of the façade system was built and its thermal performance measured. This full-scale model was used as a first approach to the new façade system. Next, some of its parameters were rethought and improved in subsequent stages of the design and analysis process. In parallel to these tests, experimental measurements were carried out in order to obtain the values of emissivity for the photocatalytic coating used on the slats. At the same time, a computational fluid dynamics (CFD) digital twin of the façade was built and validated against the experimental results previously obtained. This digital model was used first to check and improve the internal aerodynamics of the slats, as some parameters of the scale model relating to airflow performance were found to be improvable. Once the operating conditions were established, they were used to test the system under different environmental conditions in order to evaluate its application range. The results obtained show that the geographical areas where the proposed façade system would be best able to exploit the full potential of filtering and passive preheating of intake air would be temperate or cold areas with many hours of solar radiation. The system can incorporate add-ons and modifications that would enable it to be used to advantage even during warm periods.

2. Model Thermal Performance Tests

2.1. Methodology for Thermal Model

In order to evaluate the thermal performance of the façade system, a physical model of the double skin façade (DSF) was built. The model was 50 cm wide with prismatic geometry. Two 6 mm glass layers were used for the front and rear faces enclosing a 20 cm deep ventilated air cavity, as shown in Figure 1. The lateral enclosure walls consisted of a 19 mm softwood layer covered with expanded polystyrene (EPS) 40 mm thick. The thermal resistance of the enclosing walls was significantly higher than the glazing, so they can be considered as adiabatic surfaces. Table 1 shows the thermal and optical characteristics of these external walls.

Table 1. Physical characteristics of the model's envelope materials. Source: provided by Ariño Duglass [40] and from CTE [41].

	Front Glazing	Rear Glazing	Opaque Surfaces
	Extra-clear	Colourless	Softwood + EPS
Thickness	6 mm	6 mm	19 mm + 40 mm
Light transmission	91%	20%	-
Exterior light reflection	8%	32%	-
U value	5.7 W/m^{2}K	5.2 W/m^{2}K	0.68 W/m^{2}K
Solar factor	27%	27%	-
UV transmission	69%	11%	-
UV reflection	8%	32%	-

The air inlet opening (2.5 cm height) is located in the lower front side of the model, while the outlet (4 cm height) is in the upper rear side. In the case of a real façade, the air expelled through this outlet would enter the building to ventilate the interior living space, while in the case of the model, it was discharged into the atmosphere (Figures 1 and 2).

Inside the double skin cavity, five louvres were placed as shown in Figure 1 (marked as L1 to L5). These louvres (Figure 3) consisted of two overlapping sheets of balsa wood each 1.5 mm thick and cardboard slats with openings in the front and rear ends, so the airflow is forced to circulate through the slats. All the joints with the perimeter walls and glazing were sealed with silicone sealant and compressible foam bands in order to prevent air

leakage. ProClean-Air photocatalytic coating [42] was applied to the upper slat's exterior face, with an estimated solar absorption of 0.20 [43].
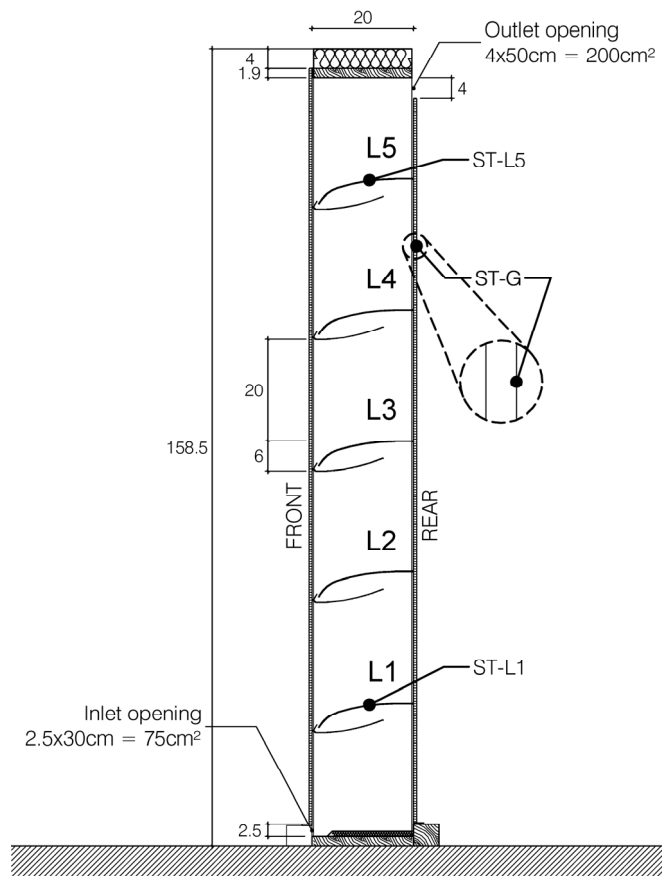

Figure 1. Dimensions of the model and location of the sensors (units in cm).

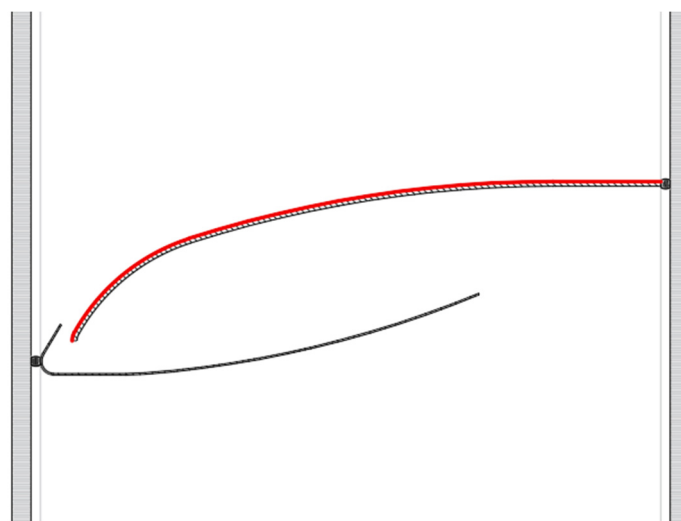**Figure 2.** Model installed at the testing site.

Figure 3. Detail of the model louvres, in red, the photocatalytic coating.

The model was placed on the terrace of the Escola Tècnica Superior d'Arquitectura de Barcelona (UPC-ETSAB; Barcelona, Spain), with the front glazing facing south (Figure 1), thus guaranteeing the photocatalytic coating's exposure to solar radiation. Nearby buildings would cast shade on the model in the early morning and late afternoon hours. Direct sunlight exposure and shaded periods during the test dates are shown in Table 2.

Table 2. Sunlight exposure periods during the tests.

Date	Indirect Sunlight	Direct Sunlight	Indirect Sunlight
3 October 2019 (UTC + 2 h)	7:45–9:00	9:00–17:00	17:00–19:30
15 January 2020 (UTC + 1 h)	8:15–9:30	9:30–15:15	15:15–17:45

The model was tested under free convection regime for warm and cold outdoor temperature conditions. From these periods, 2 days with clear sky were selected—3 October 2019 and 15 January 2020. The outdoor conditions were obtained from the Barcelona Zona Universitària XEMA weather station (at 300 m from the model), whose registers are accessible through the Generalitat de Catalunya Open Data Portal [44].

Temperatures were measured and recorded using NTC 100K 3950 Thermistors connected to an Arduino UNO board [45]. The set was previously calibrated for the expected measured temperature range (0 °C to 75 °C), with an accuracy of 1% and 0.25 °C and a resolution of 0.1 °C. The location of these sensors is shown in Figure 1; ST* sensors, graphed in black, measured surface temperatures (ST-L louvre surface temperatures and ST-G glass surface temperatures), while AT* sensors, graphed in grey, measured airstream temperatures.

2.2. Results and Discussion of the Thermal Model

The temperatures measured on the model were registered every 30 s, but, in order to analyse the temperature variation across the whole day, these readings were converted to 15-min moving averages in order to reduce fluctuations, as shown in Figures 4 and 5.

As can be seen, the maximum temperature inside the ventilated cavity is around 44 °C and 32 °C in warm and cold outdoor temperature conditions respectively. Comparing the highest internal temperature with external air temperature gives temperature differences of about 20 °C in October and 17 °C in January. While this overheating is not desirable for operation in summer, during winter it would appreciably pre-heat the intake ventilation air.
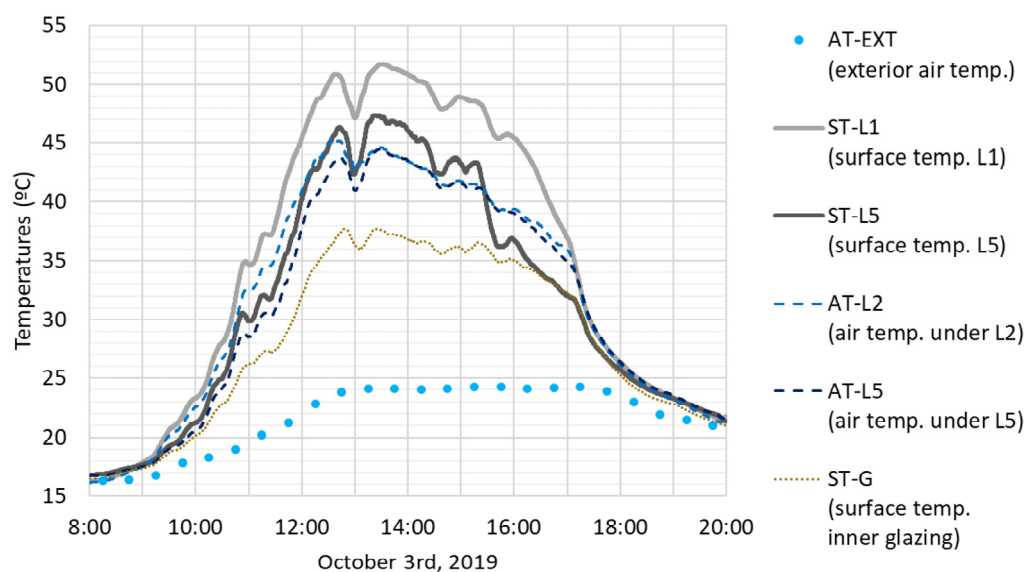
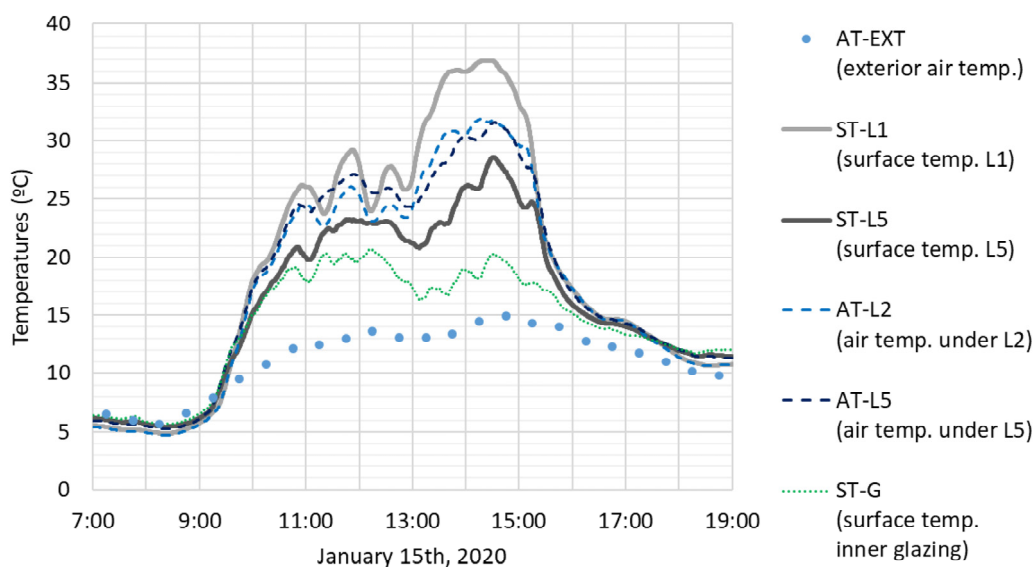**Figure 4.** Temperatures in the model during the selected day in warm outdoor temperature conditions.

Figure 5. Temperatures in the model during the selected day in cold outdoor temperature conditions.

The fact that the air temperature under louvre 2 and under louvre 5 are so similar, as can be seen in Figures 4 and 5, (1.0 °C average of absolute difference during the depicted period in October and 0.8 °C in January) suggests that the air inside the cavity practically stagnates, which means very low air circulation. This is due to the frictional and dynamic pressure losses related to the intricate path that the air has to follow through the louvres. These results indicate that, under these experimental conditions, natural ventilation with thermal buoyancy is the dominating force, but this alone might be unable to overcome the pressure losses inside the cavity. Therefore, forced ventilation would be necessary to move the air through the DSF.

The recordings were taken under free convection regime; the terrace floor surroundings, balustrade, and nearby façades (Figure 2) are clad with thin, red ceramic brick with an estimated short-wavelength absorptance higher than 0.5 [46,47]. Considering that the recorded surface temperature of slat L1 is higher than that of slat L5, this indicates the presence of irregular diffuse and reflected radiation on the model: the lower slat receives more reflected and emitted radiation from the surroundings than slat L5. Slat L5 is located

above the level of the balustrade (which is 105 cm high) and oriented upwards, it therefore does not receive radiation reflected and emitted from the balustrade.

These experimental considerations lead to the definition of a CFD model for analysing the performance of the cavity airflow under different external conditions and forced airflow. This CFD model is useful for evaluating the façade system viability, as well as improving the slat geometry, according to the airflow in the cavity.

3. Photocatalytic Coating Emissivity Tests

In order to perform the thermal characterization of the façade system through a CFD model, it is necessary to know the values of its characteristic parameters. Among them, the long-wave emissivity of the photocatalytic coating used in the façade slats was unknown: this value is not provided on the manufacturer's datasheet [42]. The literature consulted showed disperse, and in some cases, contradictory, composition-dependent data for this kind of coating, so this could not be used as a reliable source [48–50]. For this reason, a test was carried out to measure the long-wave emissivity of the coating.

3.1. Methodology for Emissivity Tests

Four ceramic samples (10 × 10 × 0.5 cm) were prepared by applying two layers of ProClean-Air photocatalytic coating [42], with a 24-h activation period, according to the manufacturer's instructions. Samples were then exposed to direct sunlight while recording their surface temperatures using both surface thermistors and a thermographic camera. Measurements were taken at an outdoor terrace at the Escola d'Enginyeria Barcelona Est (UPC-EEBE; Barcelona, Spain) on 20 July 2020 around 4:00 pm. During the test, the ambient temperature was 27 °C, and the global radiation on horizontal surfaces was 823 W/m^2, obtained from XEMA weather station Badalona-Museu, located 4 km north of the experimental testing site [51].

The samples were laid on a 30 mm thick XPS panel to minimize heat transfer to and from the support surface. The upper surfaces of the samples were exposed to direct and diffuse solar radiation and were in contact with air at ambient temperature (Figure 6).
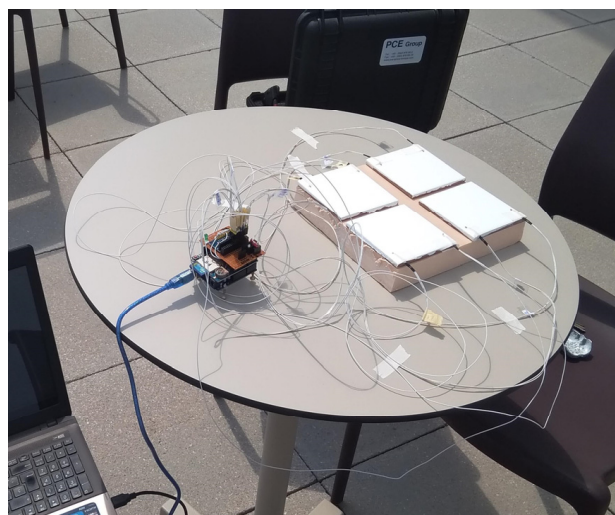

Figure 6. General view of the emissivity experimental set-up.

Surface temperatures of the samples were measured with NTC 100K 3950 thermistors connected to an Arduino UNO board [45], previously calibrated for the expected temperature range (0 °C to 75 °C); two sensors were placed on each sample (Figures 6 and 7a). Simultaneously, thermographic photographs were taken with the thermographic camera PCE-TC 3 [52]. The technical specifications of these elements are detailed in Table 3.
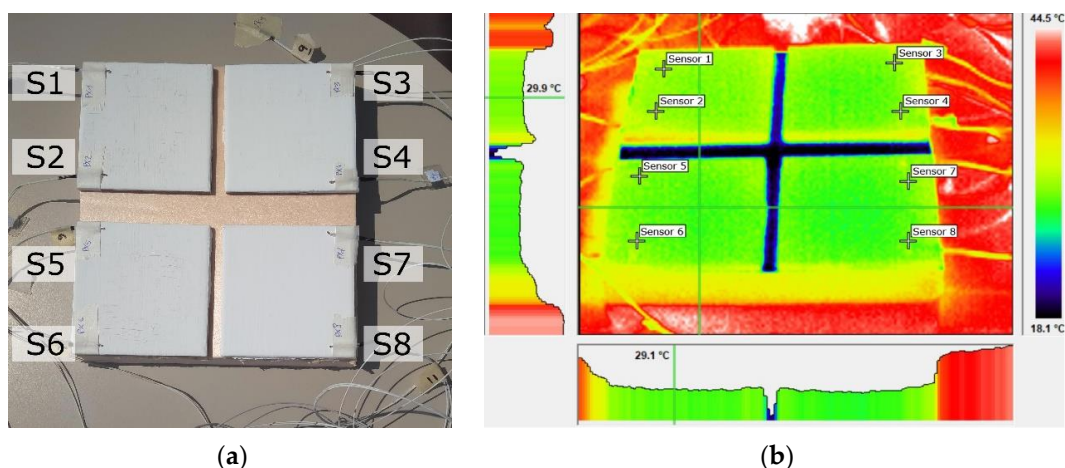
(**a**)   (**b**)

Figure 7. Position of NTC sensors (**a**), and thermographic picture E10 after adjusting the emissivity (**b**).

Table 3. Technical specifications of the measuring devices used [52,53].

Device	Model	Accuracy	Measuring Range	Resolution
Thermistor	NTC 100K 3950	±1% ±0.25 °C	−50 °C to 260 °C (max. expected measuring range 0 °C to 75 °C)	0.1 °C
Thermographic camera	PCE-TC 3	±2% ±2 °C	−10 to 250 °C	0.15 °C

After synchronizing the clocks of the thermographic camera and the Arduino UNO board, a series of thermographic pictures of the samples were taken in order to estimate the emissivity of the photocatalytic coating at ambient temperature. At the same time, surface temperatures measured by the thermistors were recorded by the Arduino UNO board. The time stamp on the thermographic pictures was used to retrieve the corresponding measured temperature data. The NTC recorded temperature data was used to adjust the sample's emissivity reading using the camera's data processing software (e.g., Figure 7b), until the average temperature fell within the measured range. The effects of reflected temperature were accounted for in the camera's processing software [52].

3.2. Results and Discussion for Emissivity Tests

Ten different thermographic pictures (Experiments E01 to E10) were taken in order to guarantee the fairness of the results. Table 4 shows the obtained surface temperatures for the thermistors, numbered according to Figure 7a.

Table 4. Temperatures (in °C) recorded by the NTC sensors (S1–S8) at the same moment of every thermographic picture (E01–E10).

		Sensors								Average and Standard Deviation
		S1	S2	S3	S4	S5	S6	S7	S8	
Experiments	E01	29.90	30.36	30.05	29.94	30.35	30.48	30.64	30.37	30.26 ± 0.27
	E02	29.62	30.35	29.53	29.53	30.08	30.14	30.13	29.90	29.91 ± 0.32
	E03	29.71	30.35	30.45	29.90	30.17	30.44	30.49	30.18	30.21 ± 0.28
	E04	29.19	29.71	29.62	29.25	29.80	30.03	29.73	29.73	29.63 ± 0.28
	E05	29.30	29.99	29.07	29.16	29.62	29.71	29.62	29.53	29.50 ± 0.31
	E06	29.36	30.08	29.35	29.25	29.80	29.82	29.76	29.44	29.61 ± 0.30
	E07	29.17	29.43	29.53	29.07	29.67	29.80	29.62	29.62	29.49 ± 0.25
	E08	29.86	30.26	30.08	30.17	30.17	30.56	30.61	30.45	30.27 ± 0.26
	E09	29.89	30.64	30.16	29.62	30.26	30.45	30.36	30.18	30.20 ± 0.32
	E10	29.49	30.26	29.52	29.34	29.90	30.05	29.89	29.72	29.77 ± 0.31

Table 5 shows the results obtained for the emissivity of the photocatalytic coating in every experiment, together with the calculation of the uncertainty of the average value: average emissivity of 0.59 with an uncertainty of 0.13.

Table 5. Obtained long-wave emissivity for the samples.

Exp.	ε_{TG}	ε_{avg}	Deviation	Average Deviation	Sensor Precision	Maximal Deviation	Standard Deviation	Uncertainty
E01	0.43		0.16					
E02	0.49		0.10					
E03	0.60		0.01					
E04	0.50		0.09					
E05	0.62		0.03					
E06	0.43	**0.59**	0.16	0.10	0.01	0.18	0.13	**0.13**
E07	0.79		0.20					
E08	0.70		0.11					
E09	0.74		0.15					
E10	0.57		0.02					

4. Façade System CFD Model

CFD has proved to be a powerful tool for understanding the flow dynamics and heat/mass transfer phenomena in the built environment [54–57], and it has been widely applied to the study of VDSF [58]. Previous experiments on the subject by this research group include the validation of numerical sub-models for CFD VDFS simulations [21,59–61] and parametric and operating studies of VDSF with louvres [23,24].

A CFD model of the experimental setup described in Section 2 was built in order to improve the aerodynamic performance and to test the thermal behaviour of the façade module. First, a 3-stage grid refinement study was performed in order to ensure the numerical independence of the results. The independent grid obtained was validated against the experimental results shown in Section 2.

In order to reduce the model size and thus the computational cost of the simulations, some geometric simplifications were made. The computational model has a differential width of 5 mm and symmetrical boundary conditions on its lateral faces, effectively simplifying the geometry to a thin central slice of the experimental model (Figure 8).

4.1. Mesh Independency

For this study, the grid convergence index (GCI) was estimated for a series of successive, systematic grid refinements, following the method introduced by Roache [62], until the solution was found to be within the asymptotic range of convergence.

For all cases, a hexahedral-dominant mesh (Figure 8) was built and tested under flow and thermal steady-state conditions. The flow was taken to be incompressible and in turbulent regime (Re $\cong$ 4500 in the inter-louver channel). The ventilation flow rate at the inlet opening was set to 18.25 l/s per meter of façade [63], and the outlet opening was set to atmospheric pressure. Outdoor temperature and irradiance were set to the experimental values measured on 3 October 2019 at 11:00 h (shown in Section 2). The long-wave emissivity of the photocatalytic coating found in Section 3 was assigned to the corresponding surfaces of each louvre, and the thermal and optical properties of the different elements of the system were assigned, as indicated in Table 1.

The Navier–Stokes equations and the energy conservation equation, together with the surface-to-surface (S2S) radiation model and the SST $k - \omega$ turbulence model, were solved in the computational domain by means of CFD. Second order discretization schemes were used for all computed variables, and residuals $\leq 1 \times 10^{-3}$ were used in all cases as convergence criteria. The computational simulations were carried out on Ansys Fluent 2020 R2 [64] on a 64-bit, Intel core i7 processor (6 core | 12 thread) at 3.3 GHz and 32GB RAM. The thermophysical properties of the air were set to be temperature-dependent, using the

ideal gas law for density, the power law for viscosity, and the temperature-dependent polynomial for heat capacity and thermal conductivity. Solar irradiance was imposed to the model by means of the software's solar calculator [64].
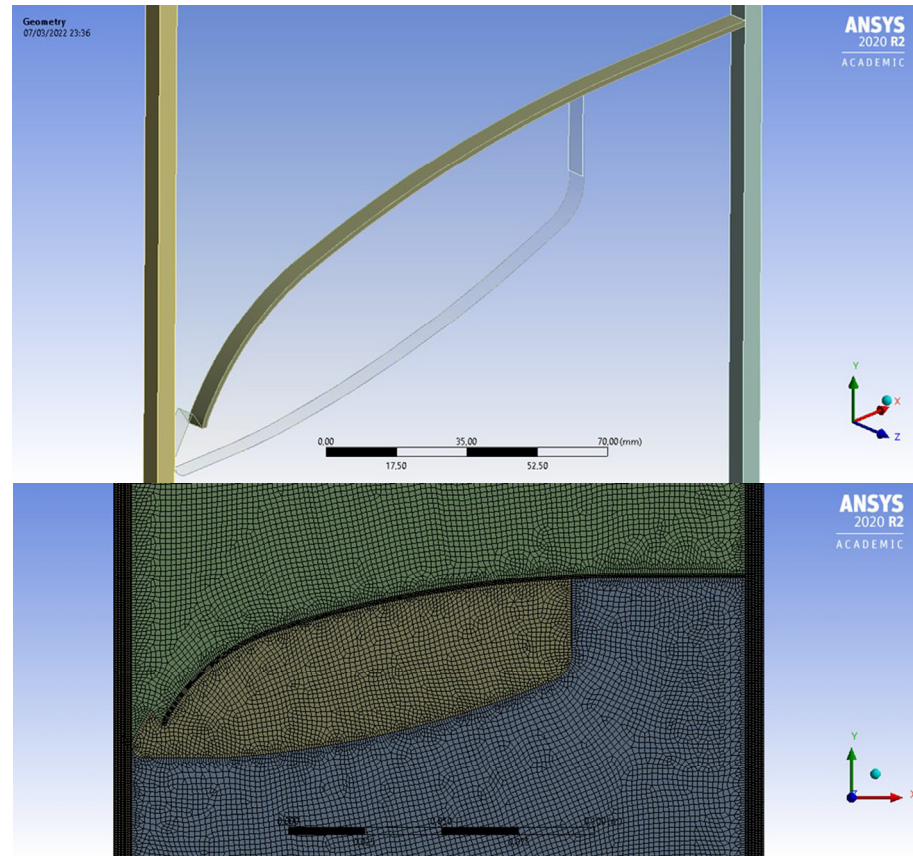

Figure 8. Details of the geometry (**top**) and mesh (**bottom**) for the CFD model.

A grid refinement study was performed first for the solid volumes (glazing, louvres, bases). Once a solid mesh size was selected, a second study was carried out for the fluid volumes (interior air), and, lastly, the mesh size in the perpendicular direction of the section was also studied, as the 3D mesh was created as an extrusion of a 2D surface mesh. Table 6 shows the grid refinement studies and the selected mesh sizes (highlighted in grey). The resulting mesh had 3.16 million hexahedral elements and 14.1 million nodes.

Table 6. Results of the grid refinement studies.

MESH SENSITIVITY ANALYSIS												
Solid mesh	*size ratio*	1.4142										
Mesh	**Element size (mm)**			**Average temperatures (K)**				**GRID REFINEMENT STUDY**				
	Fluid	**Solid**	**z-axis**	**Inner glass**	**Slat 1**	**Slat 5**	**Int. air**	ε	$\lvert p \rvert$	**GCI**	**Asymptotic range of convergence (R = 1)**	
1		0.250		309.14	306.28	315.47	309.71	0.0001	2.00	0.0001	1.00	
2		**0.354**		309.24	306.28	315.64	309.73					
3	1.000	0.500	1.250	309.21	306.26	315.61	309.70	0.0001	2.00	0.0001		0.63
4		0.707		308.88	304.61	315.06	309.61	0.0003	2.74	0.0002		0.38
5		1.000		309.29	306.30	315.58	310.05	0.0014	4.74	0.0004		

Table 6. *Cont.*

MESH SENSITIVITY ANALYSIS

Fluid mesh	*size ratio*	1.4142

Mesh	Element size (mm)			Average temperatures (K)				GRID REFINEMENT STUDY				
	Fluid	Solid	z-axis	Inner glass	Slat 1	Slat 5	Int. air	ε	|p|	GCI	Asymptotic range of convergence (R = 1)	
1	0.500			308.54	306.30	314.76	309.46	0.0017	2.19	0.0039	1.00	
2	**0.707**			308.88	304.64	314.49	309.97					2.20
3	1.000	0.354	1.250	309.24	306.28	315.64	309.73	0.0008	2.19	0.0018		
4	1.414			308.96	304.54	315.32	309.43	0.0010	0.62	0.0050		0.01
5	2.000			308.66	305.81	314.36	309.34	0.0003	3.59	0.0001		

z-axis mesh	*size ratio*	2.0000

Mesh	Element size (mm)			Average temperatures (K)				GRID REFINEMENT STUDY				
	Fluid	Solid	z-axis	Inner glass	Slat 1	Slat 5	Int. air	ε	|p|	GCI	Asymptotic range of convergence (R = 1)	
1			0.313	308.60	304.73	313.93	309.52	0.0001	2.32	0.0001	1.00	
2			**0.625**	308.61	304.74	313.96	309.53					0.04
3	0.707	0.354	1.250	308.62	304.74	313.96	309.53	0.0000	2.32	0.0000		
4			2.500	308.59	304.74	313.93	309.50	0.0001	9.05	0.0000		24.63
5			5.000	308.60	304.73	313.93	309.51	0.0000	6.46	0.0000		

4.2. Model Validation

Once mesh independency was established, a CFD model replicating the external and operating conditions of the experiment performed on 3 October 2019 (discussed in Section 2) was configured with the purpose of validating the model setup. The obtained numerical results were compared against the recorded experimental data.

The case was taken to be transient, incompressible, and in laminar free convection flow regime (Ra $\cong 4 \times 10^7$ in the air chamber). A similar model configuration as explained in Section 4.1 was used, the only difference being that in order to model the free convection operating conditions of the experiment, both inlet and outlet were set as atmospheric openings in the computational model. Temperature was limited to a max value of 52 °C, per the recorded experimental data (Figure 4). A time step of 150 s was selected for the transient simulations, after a time step refinement study was performed on the mesh independent model selected in Section 4.1.

Temperature monitors were set in order to compare the numerical results with the aforementioned experimental data. Results are shown in Figures 9 and 10. In both cases, the CFD model reproduces to a good extent the experimental thermal behaviour measured. For the photocatalytic slats (Figure 9), the CFD model reproduces the experimental behaviour observed for the lower slat (ST-L1), while for the upper slat (ST-L5), the model predicts a behaviour similar to the lower slat. The software's solar calculator distributes the diffuse radiation evenly between all the surfaces of the model, being then unable to reproduce the diffuse radiation asymmetry conditions the experimental setup experienced.

Larger temperature differences are observed on the inner glazing temperature prediction (Figure 10). When these results are observed together with the electrical output of a 5 V 0.15 A photovoltaic (PV) cell installed next to the experimental model, it is noticeable that the underperformance of the PV cell observed after 1:00 pm corresponds in time with the larger differences in the inner glazing temperature prediction, as the computational model does not account for changing atmospheric conditions.
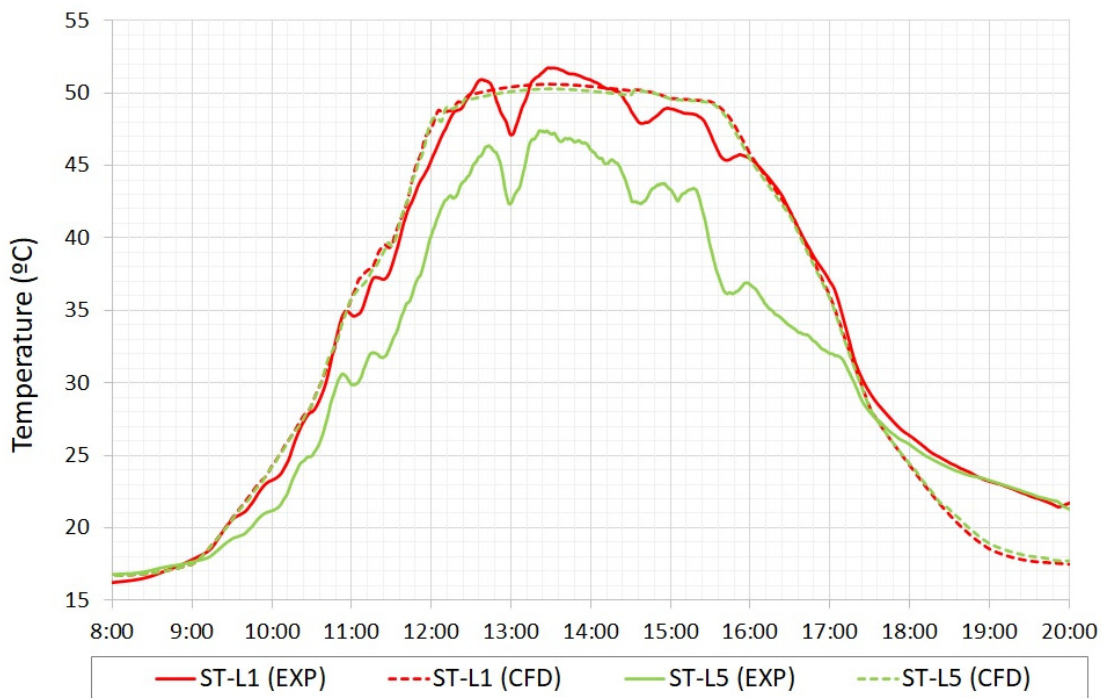
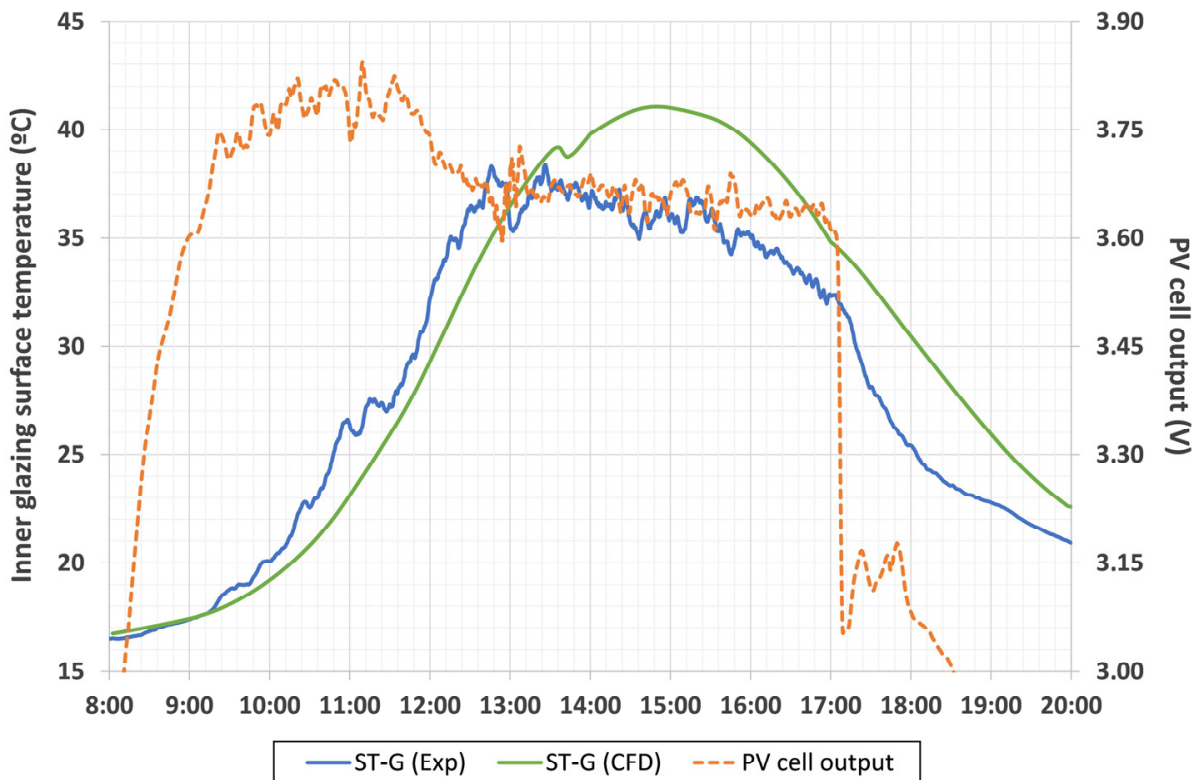**Figure 9.** Slat surface temperature validation.

Figure 10. Inner glazing temperature validation.

4.3. Model Evolution

The validated CFD model was then used to understand the shortcomings of the experimental setup and to propose and test geometry evolutions that would improve the interior aerodynamics and overall performance of the system.

Figure 11 shows a vector plot for the ventilated cavity under free convection regime. It can be observed that a low-speed ($\approx$20 cm/s) convective flow forms in the cavity between the photocatalytic slats due to the temperature difference between the inner and outer glazing. It can also be noticed that there's no significant flow in the inter-louver channel, becoming clear that the free convection, density-driven flow cannot overcome the energy losses imposed by the photocatalytic slats, remaining then stagnant in the air cavity.
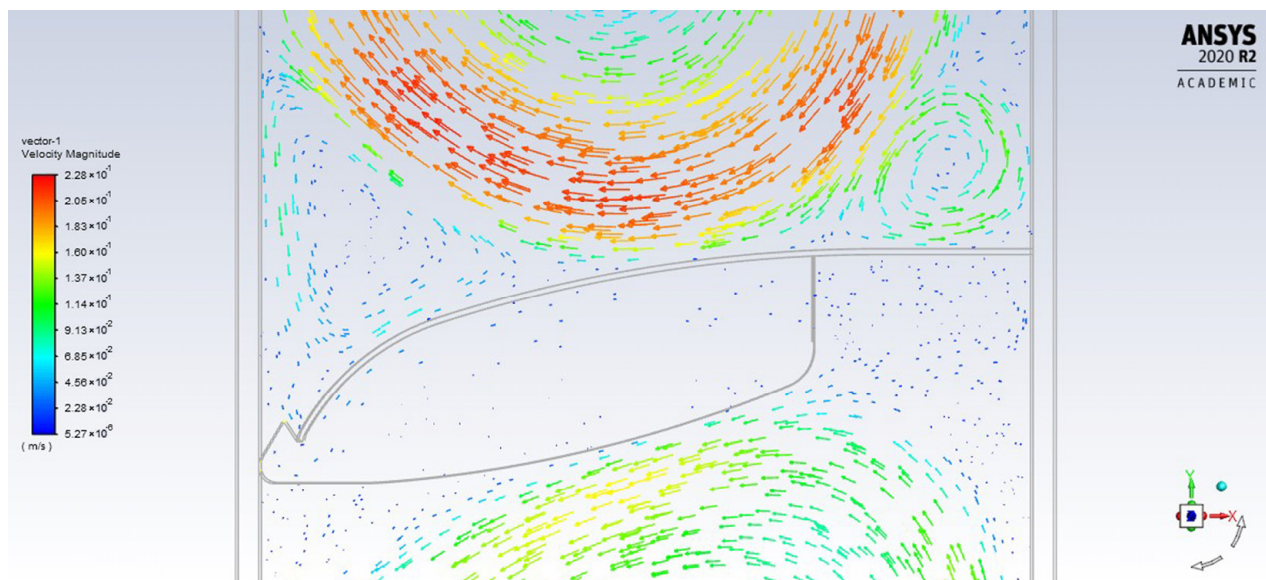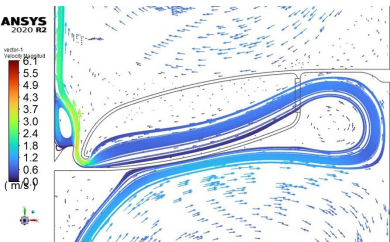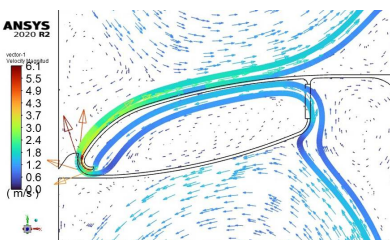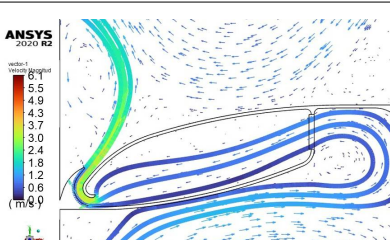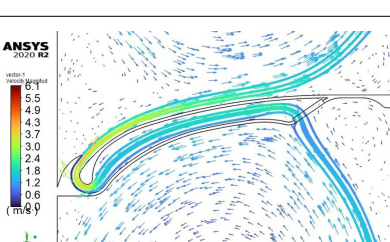

Figure 11. Velocity vectors plot in free convection operation mode.

The first evolution of the experimental setup included then mechanical ventilation, which was implemented in the CFD model by imposing a negative gauge pressure at the outlet opening (simulating the operation of a centralized air extractor). Moreover, a physical filtering stage was incorporated at the back groove of the photocatalytic slats and modelled as a porous zone. These filters were assumed to be a RESPILON$^{\circledR\circledR}$ nanofiber anti-smog window membrane RWM, with an efficiency of 95% at PM2.5, for whom pressure drop information was available [65,66]. A coupled acoustics model was also added to check for aerodynamic noise levels.

The shape of the photocatalytic slats was designed in such a way that, due to the difference of pressure generated by the high-speed flow that leaks through their front groove with respect to the air cavity, the flow would attach to the curved surface, according to the so-called Coanda effect [61,67,68]. This attached flow would favour the photocatalytic chemical reaction and therefore the decontaminating effect of the proposed façade solution. Up to 6 evolutions of the original concept were tested until satisfactory results for head losses, flow rate, aerodynamic noise levels, and flow adherence to the photocatalytic surface were reached; Table 7 summarizes the main differences between evolutions and also presents a comparison of their key operating parameters. As it can be seen, when compared to the original setup, the improved interior aerodynamics of evolution 6 reduce head losses (thus mechanical ventilation energy consumption) by 25% while increasing the ventilation flow rate (+32%) and reducing the aerodynamic noise (from 24.8 to 10.8 dB).

Table 7. Key performance indicators of the façade system.

Evolution		Ventilation Flow Rate	Gauge Pressure	Head Loss	Aerodynamic Noise	Coanda Effect?
		$\frac{l}{m_{facade} \cdot s}$	Pa	m	dB	
1		13.1	−158	13.15	24.9	Yes
2		14.6	−99	8.24	14.8	No
3		14.3	−149	12.40	20.5	No
4		12.7	−198	16.43	25.9	Yes
5		14.9	−162	13.45	10.5	No
6		17.4	−120	9.98	10.8	Yes
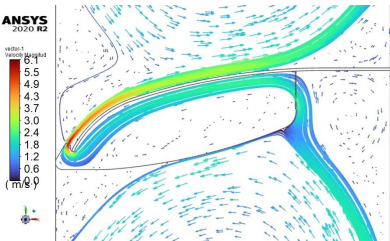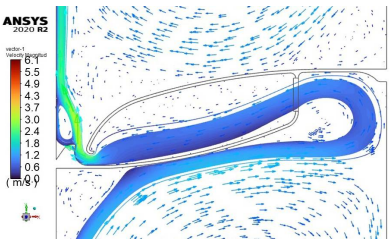
5. Range of Application of the Façade System for Different Climatic Zones

5.1. Methodology for the Range of Application Study

The improved CFD model presented in the previous section was used to test the thermal performance of the façade component under different environmental conditions in order to evaluate its range of application. It was tested under summer and winter conditions for three different climatic zones in the Northern Hemisphere: Barcelona (41.4° N), Chicago (41.9° N), and Vancouver (49.3° N); classified as Csa, Dfa, and Cfb climates, respectively, according to Köppen-Geiger climate classification [69].

For each of the cities, a representative summer and winter day were simulated. The temperatures of the representative day were obtained from open climate data for building performance simulation [70], which provides typical meteorological data derived from hourly weather data, with a historical time sequence. Individual year files were created using the general principles from the IWEC (*International Weather for Energy Calculations*) and TMY/ISO 15927-4:2005 methodologies. Among them, the specific sources chosen for our studies in Barcelona, Chicago, and Vancouver are ASHRAE/IWEC, ASHRAE/TMY3, and WYEC2, respectively. For choosing each representative day, the initial and final temperatures were confirmed to be similar. The solar radiation values were defined using the ASHRAE fair weather conditions method [71].

The simulated 24 h day cycle starts at 6:00 am to adapt to the solar cycle and to verify if the solar radiation load is given off during the night or if it is stored through the thermal inertia of the system until the following day. In all cases, the initial flow conditions at 6:00 am were set according to a prior steady-state simulation. After that, a 24 h transient simulation was run, using a 150 s time step. The flow was taken to be turbulent, incompressible, and in transient regime. A gauge pressure of -120 Pa was set at the outlet opening in order to guarantee a minimum flow rate of 15 l/m^2·s. Mesh dimensions and all other computational parameters for the model were imposed, as explained in Section 4.1.

5.2. Results and Discussion for the Applicable Range Study

As may be seen in the following graphs in Figure 12, in every one of the simulated scenarios, the temperature of the air increases while circulating through the DSF. Thus, air will be warmer when it reaches the indoor building space (outlet temperature in Figure 12) than the exterior air (inlet temperature in Figure 12), resulting in a preheated air inlet for ventilation. The fact that the initial and final temperatures at 6:00 am are very similar in all scenarios verifies that the thermal inertia of the system over the daily cycle is minimal.

In the three **summer cases**, it can be seen that during the daylight hours there is a great difference between inlet and outlet temperatures (Figure 13). The maximum difference (25.6 °C for Barcelona, 27.8 °C for Chicago, and 30.5 °C for Vancouver) is reached between 14:00 and 16:00, when the solar radiation and the external air temperature are at their highest. On the contrary, during the night hours, as the system is not affected by the incident solar radiation, the difference between inlet and outlet temperatures is mainly low and constant (an average difference of 4.0 °C for Barcelona, 2.4 °C for Chicago, and 5.6 °C for Vancouver, from 22:00 to 6:00). These trends can be seen in Figure 13, where these differences are represented graphically for the three cities analysed.

The temperature increase in the intake air during daylight hours might not be desirable in summer conditions, especially for warmer climates (Barcelona and Chicago), where it can lead to overheating of internal building spaces. For colder climates, as, for example, the case of Vancouver (where the average temperature of the representative day in summer is 15.7 °C, about 8 °C lower than Barcelona 23.1 °C and Chicago 24.7 °C), this preheating of the intake air has thermal benefits for the building—mainly early in the morning, at the end of the afternoon, and at night. We can therefore estimate that passive preheating might be desirable throughout the year for locations above 50° N.
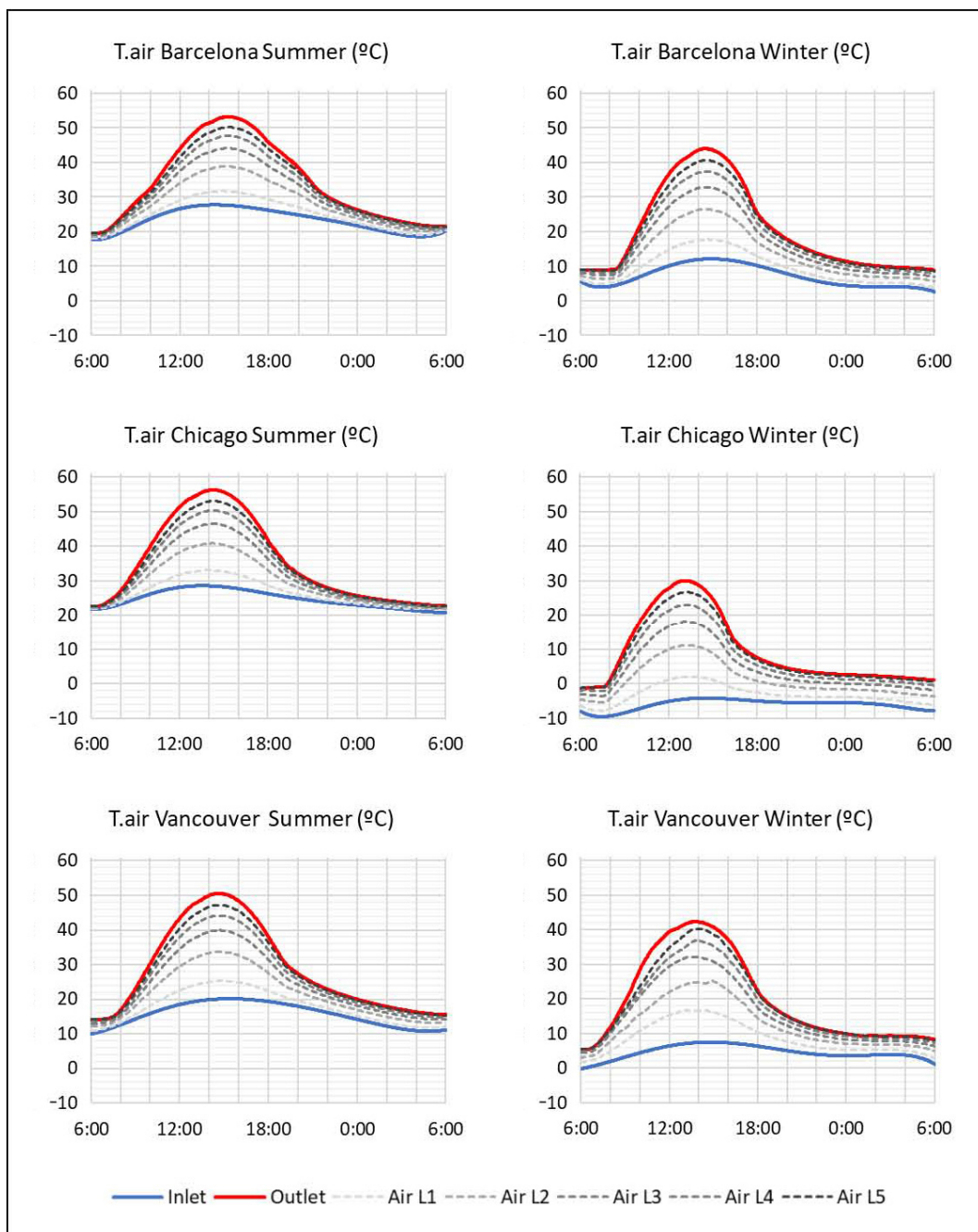
Figure 12. Temperatures of the inlet and outlet air and the air circulating through each louvre (L1 to L5).

Nevertheless, the undesirable preheating of the air in warm climates does not imply that the system should be discarded, since, during these periods, the system can be given a slightly different function to take full advantage of it: mechanically filtered free-cooling at night, solar protection to reduce the radiative heat loads and reduce the cooling demand, or even the use of this heat to assist hot water production.

By comparison, regarding the three **winter cases**, it may be seen that the system is thermally efficient 24 h per day. When the outdoor air temperature is lower than the indoor comfort temperature, the passive preheating of the air in the façade cavity is highly desirable, as it always represents an energy savings for the building's AHU system. As shown in Figure 14 and Table 8, the maximum temperature differences between inlet and outlet in all three winter cases are higher than for summer scenarios, reaching a peak of

31.9 °C for Barcelona, 34.5 °C for Chicago, and 35.0 °C for Vancouver. On a daily average, the estimated preheating for the calculated winter days is between 13.6 °C and 15.6 °C, as shown in Table 8.
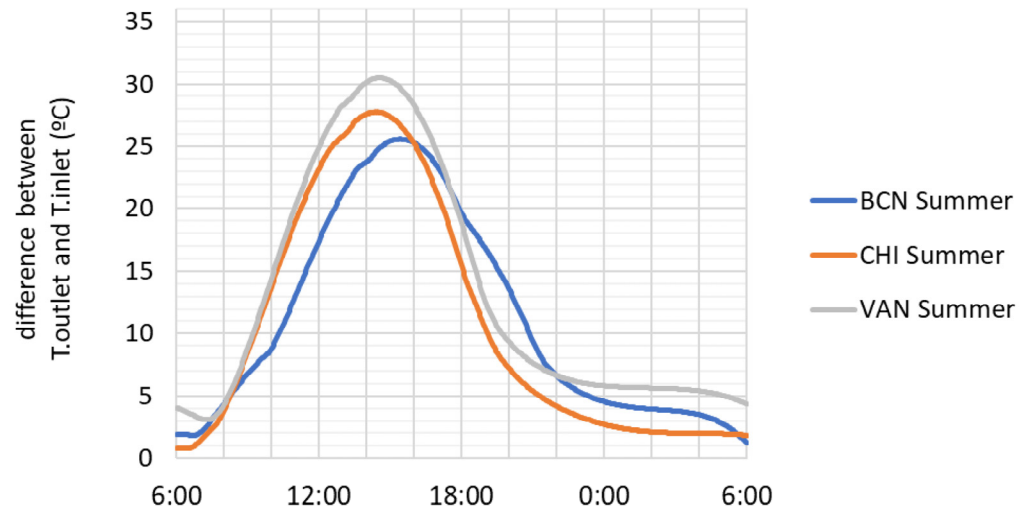

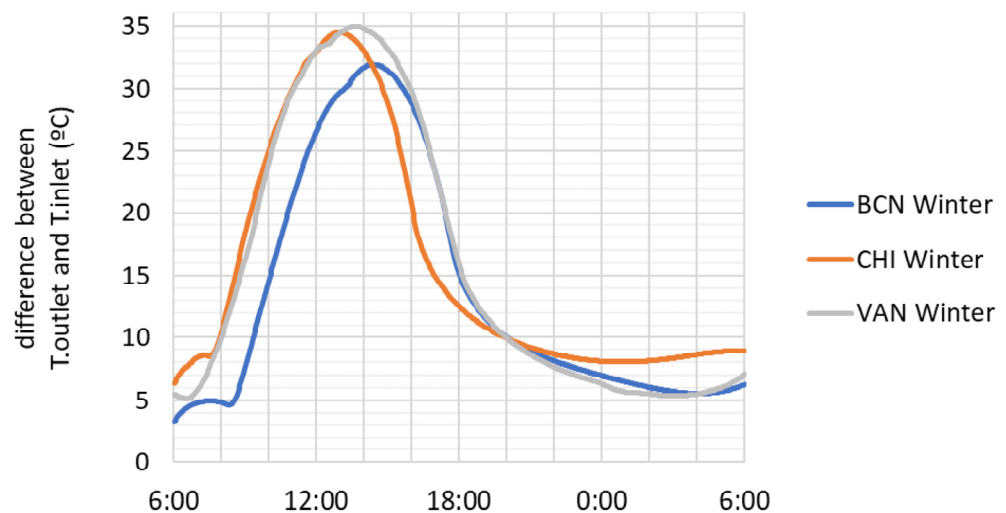**Figure 13.** Temperature difference between outlet and inlet air in summer.

Figure 14. Temperature difference between outlet and inlet air in winter.

Table 8. Maximum, average, minimum, and fluctuation of the difference of temperatures between inlet and outlet air.

	Summer			Winter		
	BCN	**CHI**	**VAN**	**BCN**	**CHI**	**VAN**
MAX.	25.6 °C	27.8 °C	30.5 °C	31.9 °C	34.5 °C	35.0 °C
Avg.	11.1 °C	10.7 °C	13.1 °C	13.6 °C	15.6 °C	15.6 °C
min.	1.2 °C	0.8 °C	3.1 °C	3.3 °C	6.4 °C	5.1 °C
fluct. MAX–min	24.4 °C	27.0 °C	27.4 °C	28.6 °C	28.1 °C	29.9 °C

In winter, the temperature differences between inlet and outlet at night are higher than in the summer; this trend is more remarkable in the most critical cases, where outdoor temperatures are lower (Chicago in the example). In Figure 14, the winter temperature differences represented for the three cities can be observed (an average difference of 6.9 °C for Barcelona, 8.6 °C for Chicago, and 6.6 °C for Vancouver, from 20:00 to 6:00). The night-time difference highlights another beneficial effect of this system: the reduction of thermal

losses. The energy that passes through the inner glazing heats the air in the cavity, which is once again reintroduced to the interior space, thus, reducing the thermal losses through the façade.

Apart from the air temperatures in the cavity, the surface temperature for the five slats has also been analysed for all the simulated cases.

As with the rest of the façade components, the louvres are heated by solar radiation. The slats in the upper section of the cavity (L5) reach higher temperatures than the ones located in lower positions (L1) (Figures 15 and 16), as they are surrounded by warmer air. This performance is observed in the three cities studied, for climatic conditions during both summer and winter.
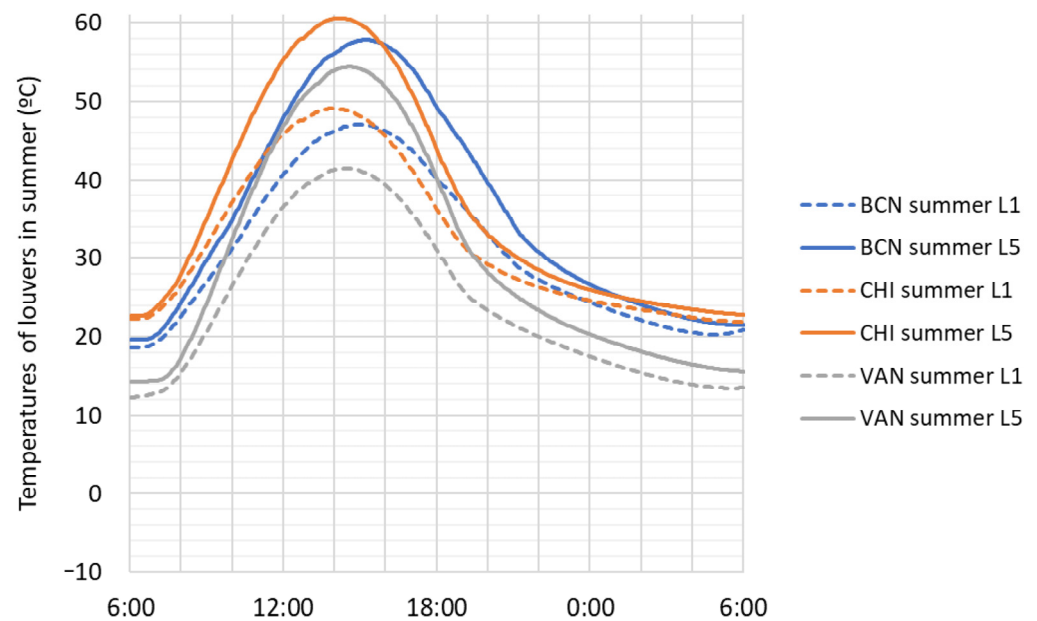

Figure 15. Temperature of the louvres on each summer day calculated.
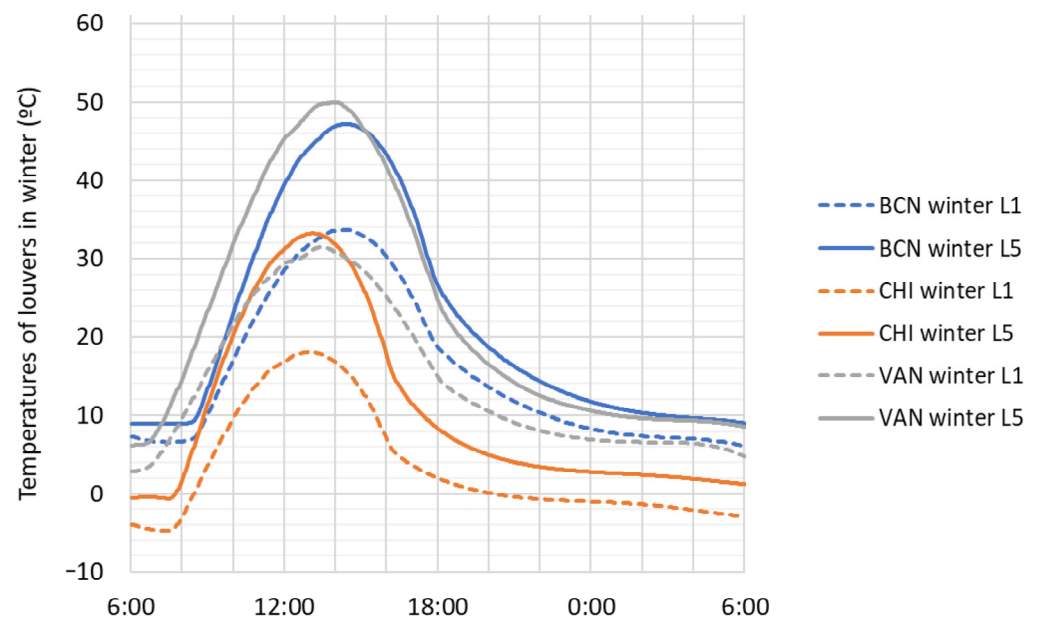

Figure 16. Temperature of the louvres on each winter day calculated.

Regarding the maximum surface temperature differences, Table 9 shows the daily average temperature range affecting the louvres for the three cities under summer and winter conditions. The case with the most extreme daily conditions is Vancouver in winter,

which presents a 43.8 °C daily temperature range, while Chicago shows the greatest annual difference (61.2 °C).

Table 9. Maximum thermal fluctuations and thermal expansion of louvres.

	Daily						Annual		
	Summer			Winter					
	BCN	CHI	VAN	BCN	CHI	VAN	BCN	CHI	VAN
max. thermal fluctuation (°C)	38.2	37.9	40.1	38.2	33.8	43.8	48.9	61.2	48.2
thermal exp. (mm/m)	0.9	0.9	0.9	0.9	0.8	1.0	1.2	1.4	1.1

The surface temperature of the slats (and also its temperature variability) is not a significant parameter in terms of the system's thermal performance, but it can be a critical factor regarding the constructional aspects of the system. The thermal fluctuations can lead to a thermal expansion phenomenon affecting the louvres, which might be made of aluminum-6061 (a common material in this type of façade element), with a linear thermal expansion coefficient of 23.4×10^{-6} °C^{-1} [72,73]. This fact must be considered when defining how the louvres are incorporated into the DSF module and how the differential movements are allowed without compromising airtightness. Although it would be advisable to study this particular aspect in detail for the final development of each building project, the following approximate calculation may help to understand the order of magnitude of this movement. The calculated daily thermal fluctuations are about 44 °C maximum, with an annual maximum of about 61 °C. These thermal fluctuations result in a daily movement of approximately 1 mm/m and an annual movement of 1.4 mm/m, as can be seen in Table 9. This means that, for a two-meter-wide module, the thermal expansion would be less than 3 mm, which is a tolerance that can be easily achieved by the system.

6. Conclusions

The proposed module is a double skin façade system that filters part of the pollutants from the ventilation intake air without the user losing the sense of freedom to open the window at will. The air purification system consists of a set of fixed slats housed within the cavity, which provide both physical and photocatalytic filtering. The slats also provide solar protection for the interior of the building.

In order to evaluate the thermal performance of the façade system, a 1:1 scale model of a DSF under free convection regime was built and tested for warm and cold outdoor temperature conditions in Barcelona. It was found that, under these experimental conditions, using natural ventilation alone with thermal buoyancy as the dominating driving force, it might not be possible to overcome the frictional and dynamic losses through the louvres. Consequently, forced ventilation would be necessary to move the air through the DSF.

The long-wave emissivity of the ProClean-Air photocatalytic coating used in the façade slats was an unknown characteristic parameter, but it was required in order to study the thermal performance of the façade system. For this reason, a test was carried out to estimate the emissivity of the coating. Four ceramic samples coated with ProClean-Air were analysed at ambient temperature, resulting in an average value of 0.59 ± 0.13.

A CFD model of the experimental setup was built in order to improve its aerodynamic performance and to test the façade module under different climatic conditions. An independent mesh was validated against the experimental results in order to ensure the numerical independence of the results. The validated mesh was then used to improve the interior aerodynamics of the module in order to reduce frictional losses, reduce aerodynamic noise, and to ensure the Coanda flow so as to improve the photocatalytic reaction.

The thermal performance of the improved system was then computed under outdoor conditions in summer and winter for three different climatic zones in the northern hemisphere (Barcelona, Chicago, and Vancouver) to study the appropriate climatic range of application.

The increase in air temperature as the air circulates through the double skin making contact with the photocatalytic slats supposes the preheating of the intake air, which can be very positive in cold and mild periods or climates. On a daily average, the estimated preheating for the calculated days in cold periods is between 13.6 °C and 15.6 °C, while in warm days it is between 10.7 °C and 13.1 °C.

Thermal fluctuations can lead to thermal expansion phenomena affecting the louvres, which must be taken into account when designing the system for each specific situation. Within the situations studied, these thermal expansions are less than 1.5 mm/m, or less than 3 mm for a two-metre-wide module, which is a tolerance that the system may easily achieve.

In cold climates, passively preheating the filtered air would be positive throughout most of the year, but, in temperate climates, this might be undesirable during some periods of the year. The system can incorporate add-ons and modifications that would enable it to be used to advantage even during warm periods: mechanically filtering night-time intake air ventilation, solar protection, and thus the reduction of the cooling demand, or support for hot water production.

Although the potential use of this system is broad, the geographical areas where it would be best to exploit the full potential of filtering and passive preheating of the intake air would be in temperate or cold areas with many hours of solar radiation: central Europe and low latitude areas that are high above sea level.

7. Patents

A patent and a utility model were registered related to this project [74,75].

Author Contributions: Conceptualization, O.R., E.C., C.P., A.G., A.I. and J.L.-B.; Funding acquisition, C.P.; Investigation, O.R., E.C., C.P., A.G., A.I. and J.L.-B.; Methodology, O.R., E.C., C.P., A.G., A.I. and J.L.-B.; Project administration, C.P. and J.L.-B.; Supervision, C.P. and J.L.-B.; Validation, O.R., E.C., A.G. and A.I.; Visualization, O.R. and A.G.; Writing—original draft, O.R., E.C. and A.G.; Writing—review & editing, O.R., E.C., C.P., A.G., A.I. and J.L.-B. All authors have read and agreed to the published version of the manuscript.

Conflicts of Interest: The authors declare no conflict of interest. The funders had no role in the design of the study; in the collection, analyses, or interpretation of data; in the writing of the manuscript; or in the decision to publish the results.

Acronyms and Abbreviations

AHU	Air Handling Unit (Air Treatment Unit)
CFD	Computational Fluid Dynamics
CTE	Código Técnico de la Edificación (Spanish building regulation)
DSF	Double Skin Façade
EPS	Expanded Polystyrene
GCI	Grid Convergence Index
IAQ	Indoor Air Quality
NTC sensor	Negative Temperature Coefficient sensor
UPC-EEBE	Universitat Politècnica de Catalunya—Escola d'Enginyeria Barcelona Est
UPC-ETSAB	Universitat Politècnica de Catalunya—Escola Tècnica Superior d'Arquitectura de Barcelona
UV	Ultraviolet
VDSF	Ventilated Double Skin Façades

VOCs	Volatile Organic Compounds
XPS	Extruded Polystyrene

References

1. Velux The Indoor Generation. The Effects of Modern Indoor Living on Health, Wellbeing and Productivity. YouGov Survey—Read More about How Life Indoor Effects Us. Available online: https://www.velux.com/indoorgeneration (accessed on 14 July 2021).
2. Ortiz, M.; Itard, L.; Bluyssen, P.M. Indoor Environmental Quality Related Risk Factors with Energy-Efficient Retrofitting of Housing: A Literature Review. *Energy Build.* **2020**, *221*, 110102. [CrossRef]
3. Office of the United Nations High Commissioner for Humar Rights the Right to Adequate Housing. Fact Sheet 21. 2009. Available online: https://www.ohchr.org/sites/default/files/Documents/Publications/FS21_rev_1_Housing_en.pdf (accessed on 9 January 2023).
4. Khovalyg, D.; Kazanci, O.B.; Halvorsen, H.; Gundlach, I.; Bahnfleth, W.P.; Toftum, J.; Olesen, B.W. Critical Review of Standards for Indoor Thermal Environment and Air Quality. *Energy Build.* **2020**, *213*, 109819. [CrossRef]
5. Wei, W.; Ramalho, O.; Mandin, C. Indoor Air Quality Requirements in Green Building Certifications. *Build. Environ.* **2015**, *92*, 10–19. [CrossRef]
6. Grün, G.; Urlaub, S.; Foldbjerg, P. *Part A: Towards an Identification of European Indoor Environments' Impact on Health and Performance—Mould and Dampness*; Fraunhofer IBP: Stuttgart, Germany, 2016.
7. Brager, G.S.; Paliaga, G.; De Dear, R.; Olesen, B.; Wen, J.; Nicol, F.; Humphreys, M. Operable Windows, Personal Control, and Occupant Comfort. *Ashrae Trans.* **2004**, *110*, 17–35.
8. De Dear, R.J.; Brager, G.S. Thermal Comfort in Naturally Ventilated Buildings: Revisions to ASHRAE Standard 55. *Energy Build.* **2002**, *34*, 549–561. [CrossRef]
9. Luo, M.; Cao, B.; Ji, W.; Ouyang, Q.; Lin, B.; Zhu, Y. The Underlying Linkage between Personal Control and Thermal Comfort: Psychological or Physical Effects? *Energy Build.* **2016**, *111*, 56–63. [CrossRef]
10. Luna-Navarro, A.; Loonen, R.; Juaristi, M.; Monge-Barrio, A.; Attia, S.; Overend, M. Occupant-Facade Interaction: A Review and Classification Scheme. *Build. Environ.* **2020**, *177*, 106880. [CrossRef]
11. Neila González, F.J. *Arquitectura Bioclimática En Un Entorno Sostenible*; Munillaleria: Madrid, Spain, 2004; ISBN 9788489150645.
12. Allard, F. *Natural Ventilation in Buildings: A Design Handbook*; James and James (Science Publishers) Ltd.: London, UK, 1998; ISBN 9781873936726.
13. Năstase, G.; Doboși, I.S.; Brezeanu, A.I.; Taus, D.; Tăbăcaru, M.B.; Vuțoiu, B.G.; Rusu, D.; Bulmez, A.M.; Iordan, N.F. Experimental Heat Transfer, Sound Insulation and Interior Comfort Parameters Assessment on a Box Double-Skin Façade. *Buildings* **2022**, *12*, 730. [CrossRef]
14. Poirazis, H. *Double Skin Facades for Office Buildings—Literature Review Report*; Lund Institute of Technology: Lund, Switzerland, 2004; ISBN 91-85147-02-8.
15. Zelenay, K.; Perepelitza, M.; Lehrer, D. *High-Performance Facades Design Strategies and Applications in North America and Northern Europe*; Center for the Built Environment: Berkeley, CA, USA, 2011.
16. Gratia, E.; De Herde, A. Is Day Natural Ventilation Still Possible in Office Buildings with a Double-Skin Façade? *Build. Environ.* **2004**, *39*, 399–409. [CrossRef]
17. Gratia, E.; De Herde, A. Natural Cooling Strategies Efficiency in an Office Building with a Double-Skin Façade. *Energy Build.* **2004**, *36*, 1139–1152. [CrossRef]
18. Manz, H.; Frank, T. Thermal Simulation of Buildings with Double-Skin Façades. *Energy Build.* **2005**, *37*, 1114–1121. [CrossRef]
19. Karadag, I.; Cakmakli, A.B. Interface of the Natural Ventilation Systems with Building Management Systems. *Period. Polytech. Archit.* **2020**, *51*, 178–188. [CrossRef]
20. Saroglou, T.; Theodosiou, T.; Givoni, B.; Meir, I.A. A Study of Different Envelope Scenarios towards Low Carbon High-Rise Buildings in the Mediterranean Climate—Can DSF Be Part of the Solution? *Renew. Sustain. Energy Rev.* **2019**, *113*, 109237. [CrossRef]
21. Guardo, A.; Coussirat, M.; Egusquiza, E.; Alavedra, P.; Castilla, R. A CFD Approach to Evaluate the Influence of Construction and Operation Parameters on the Performance of Active Transparent Façades in Mediterranean Climates. *Energy Build.* **2009**, *41*, 534–542. [CrossRef]
22. Torres, M.; Alavedra, P.; Guzmán, A.; Cuerva, E.; Planas, C. Double Skin Façades—Cavity and Exterior Openings Dimensions for Saving Energy on Mediterranean Climate. In *Building Simulation*; 2007; pp. 198–205. Available online: https://publications.ibpsa.org/conference/paper/?id=bs2007_407 (accessed on 22 December 2022).
23. Parra, J.; Guardo, A.; Egusquiza, E.; Alavedra, P. Thermal Performance of Ventilated Double Skin Façades with Venetian Blinds. *Energies* **2015**, *8*, 4882–4898. [CrossRef]
24. Velasco, A.; García, S.J.; Guardo, A.; Fontanals, A.; Egusquiza, M. Assessment of the Use of Venetian Blinds as Solar Thermal Collectors in Double Skin Facades in Mediterranean Climates. *Energies* **2017**, *10*, 1825. [CrossRef]
25. Planas, C.; Cuerva, E.; Alavedra, P. Effects of the Type of Facade on the Energy Performance of Office Buildings Representative of the City of Barcelona. *Ain Shams Eng. J.* **2018**, *9*, 3325–3334. [CrossRef]
26. World Health Organization (WHO); Climate & Clean Air Coalition (CCAC). BreathLife: The Equation Is Simple. 2015. Available online: https://www.who.int/publications/m/item/breathlife-equation-is-simple (accessed on 9 January 2023).

27. Breathe Life 2030—Health and Climate Impacts. Available online: https://breathelife2030.org/the-issue/health-and-climate-impacts/?playlearn (accessed on 14 July 2021).

28. Li, H.; Zhong, K.; Zhai, Z. A New Double-Skin Façade System Integrated with TiO_2 Plates for Decomposing BTEX. *Build. Environ.* **2020**, *180*, 107037. [CrossRef]

29. Flores Lazo, J.F. Integración En Fachada de Mecanismos de Depuración de Aire. Master's Thesis, Universitat Politècnica de Catalunya, Barcelona, Brazil, 2018.

30. Coronado, J.M.; Portela, R.; Hernández-Alonso, M.D.; García Rodríguez, S.; Fresno García, F.; Suárez Gil, S.; de la Peña O'Shea, V.A. *Design of Advanced Photocatalytic Materials for Energy and Environmental Applications*; Coronado, J.M., Fresno García, F., Hernández-Alonso, M.D., Portela, R., Eds.; Springer: Berlin/Heidelberg, Germany, 2013; ISBN 978-1-4471-5060-2.

31. Lee, J.E.; Ok, Y.S.; Tsang, D.C.W.; Song, J.H.; Jung, S.C.; Park, Y.K. Recent Advances in Volatile Organic Compounds Abatement by Catalysis and Catalytic Hybrid Processes: A Critical Review. *Sci. Total Environ.* **2020**, *719*, 137405. [CrossRef]

32. Maness, P.C.; Smolinski, S.; Blake, D.M.; Huang, Z.; Wolfrum, E.J.; Jacoby, W.A. Bactericidal Activity of Photocatalytic TiO_2 Reaction: Toward an Understanding of Its Killing Mechanism. *Appl. Environ. Microbiol.* **1999**, *65*, 4094–4098. [CrossRef]

33. Chen, D.; Li, F.; Ray, A.K. Effect of Mass Transfer and Catalyst Layer Thickness on Photocatalytic Reaction. *AIChE J.* **2000**, *46*, 1034–1045. [CrossRef]

34. Knaack, U.; Klein, T.; Bilow, M.; Auer, T. *Façades: Principles of Construction Second and Revised Edition*; Birkhäuser: Berlin, Germany, 2014.

35. Prieto, A.; Klein, T.; Knaack, U.; Auer, T. Main Perceived Barriers for the Development of Building Service Integrated Facades: Results from an Exploratory Expert Survey. *J. Build. Eng.* **2017**, *13*, 96–106. [CrossRef]

36. Quesada, G.; Rousse, D.; Dutil, Y.; Badache, M.; Hallé, S. A Comprehensive Review of Solar Facades. Transparent and Translucent Solar Facades. *Renew. Sustain. Energy Rev.* **2012**, *16*, 2643–2651. [CrossRef]

37. Sadineni, S.B.; Madala, S.; Boehm, R.F. Passive Building Energy Savings: A Review of Building Envelope Components. *Renew. Sustain. Energy Rev.* **2011**, *15*, 3617–3631. [CrossRef]

38. Carlos, J.S.; Corvacho, H. Ventilated Double Window for the Preheating of the Ventilation Air Comparison of Its Performance in a Northern and a Southern European Climate. *J. Renew. Energy* **2013**, *2013*, 290865. [CrossRef]

39. Carlos, J.S.; Corvacho, H.; Silva, P.D.; Castro-Gomes, J.P. Real Climate Experimental Study of Two Double Window Systems with Preheating of Ventilation Air. *Energy Build.* **2010**, *42*, 928–934. [CrossRef]

40. Ariño Duglass Fabricante de Vidrio a Medida | Edificios y Ferrocarril—Ariño Duglass. Available online: https://www.duglass.com/ (accessed on 15 March 2022).

41. Instituto Eduardo Torroja de Ciencias de la Construcción; CEPCO; AICIA. *Catálogo de Elementos Constructivos Del CTE*; Instituto Eduardo Torroja de Ciencias de la Construcción: Madrid, Spain, 2010.

42. Proquicesa Photocatalytic Products—Proquicesa. Available online: https://www.proquicesa.com/en/product/photocatalytic-products/ (accessed on 15 March 2022).

43. Henninger, J.H. *Solar Absorptance and Thermal Emittance of Some Common Spacecraft Thermal-Control Coatings*; NASA Technical Reports Server: Greenbelt, MD, USA, 1984; Volume 1121.

44. Servei Meteorològic de Catalunya Dades de l'estació Automàtica Barcelona—Zona Universitària, Meteocat. Available online: https://www.meteo.cat/observacions/xema/dades?codi=X8 (accessed on 14 July 2021).

45. Arduino Uno Rev3 | Arduino Official Store. Available online: https://store.arduino.cc/arduino-uno-rev3 (accessed on 14 July 2021).

46. Martín Monroy, M. Comportamiento de Cerramientos Soleados: Un Modelo de Simulacion Por Diferencias Finitas. Ph.D. Thesis, Universidad de Las Palmas de Gran Canaria, Las Palmas de Gran Canaria, Spain, 1995.

47. Engineering ToolBox Absorbed Solar Radiation. Available online: https://www.engineeringtoolbox.com/solar-radiation-absorbed-materials-d_1568.html (accessed on 14 March 2022).

48. Fernández-Mira, M.; Jimenez-Relinque, E.; Martínez, I.; Castellote, M. Evaluation of Changes in Surface Temperature of TiO_2 Functionalized Pavements at Outdoor Conditions. *Energy Build.* **2021**, *237*, 110817. [CrossRef]

49. Pan, L.; Xu, G.; Guo, T.; Zhang, B.; Xiang, S.; Fang, G.; Li, J. Study on Thermochromic-Emissivity Performance of Mn Doped TiO_2 under Temperature Fluctuations. *Infrared Phys. Technol.* **2020**, *105*, 103192. [CrossRef]

50. Xiang, S.; Xu, G.; Liu, C.; Bu, H.; Zhang, Y. Study on the Variable Color and Emissivity Properties of Co Doped TiO_2 under Temperature Fluctuations. *Opt. Mater.* **2018**, *85*, 254–260. [CrossRef]

51. Servei Meteorològic de Catalunya Dades de l'estació Automàtica Badalona—Museu, Meteocat. Available online: https://www.meteo.cat/observacions/xema/dades?codi=WU (accessed on 14 July 2021).

52. Multi-Purpose Thermal Imager PCE-TC 3 User Manual. Available online: https://d3pcsg2wjq9izr.cloudfront.net/files/44930/download/302405/PCE-TC_3_medium_quality.pdf (accessed on 9 January 2023).

53. *Specifications for NTC Thermistor*; TEM Electronic Components: Madrid, Spain, 2021; Available online: https://www.tme.eu/Document/f9d2f5e38227fc1c7d979e546ff51768/NTCM-100K-B3950.pdf (accessed on 9 January 2023).

54. Tominaga, Y.; Stathopoulos, T. CFD Simulations Can Be Adequate for the Evaluation of Snow Effects on Structures. *Build. Simul.* **2020**, *13*, 729–737. [CrossRef]

55. Mirzaei, P.A. CFD Modeling of Micro and Urban Climates: Problems to Be Solved in the New Decade. *Sustain. Cities Soc.* **2021**, *69*, 102839. [CrossRef]

56. Thordal, M.S.; Bennetsen, J.C.; Capra, S.; Koss, H.H.H. Towards a Standard CFD Setup for Wind Load Assessment of High-Rise Buildings: Part 1—Benchmark of the CAARC Building. *J. Wind Eng. Ind. Aerodyn.* **2020**, *205*, 104283. [CrossRef]
57. Thordal, M.S.; Bennetsen, J.C.; Capra, S.; Kragh, A.K.; Koss, H.H.H. Towards a Standard CFD Setup for Wind Load Assessment of High-Rise Buildings: Part 2—Blind Test of Chamfered and Rounded Corner High-Rise Buildings. *J. Wind Eng. Ind. Aerodyn.* **2020**, *205*, 104282. [CrossRef]
58. De Gracia, A.; Castell, A.; Navarro, L.; Oró, E.; Cabeza, L.F. Numerical Modelling of Ventilated Facades: A Review. *Renew. Sustain. Energy Rev.* **2013**, *22*, 539–549. [CrossRef]
59. Coussirat, M.; Guardo, A.; Jou, E.; Egusquiza, E.; Cuerva, E.; Alavedra, P. Performance and Influence of Numerical Sub-Models on the CFD Simulation of Free and Forced Convection in Double-Glazed Ventilated Façades. *Energy Build.* **2008**, *40*, 1781–1789. [CrossRef]
60. Guardo, A.; Coussirat, M.; Valero, C.; Egusquiza, E.; Alavedra, P. CFD Assessment of the Performance of Lateral Ventilation in Double Glazed Façades in Mediterranean Climates. *Energy Build.* **2011**, *43*, 2539–2547. [CrossRef]
61. Valentín, D.; Guardo, A.; Egusquiza, E.; Valero, C.; Alavedra, P. Use of Coandă Nozzles for Double Glazed Façades Forced Ventilation. *Energy Build.* **2013**, *62*, 605–614. [CrossRef]
62. Roache, P.J. Perspective: A Method for Uniform Reporting of Grid Refinement Studies. *J. Fluids Eng.* **1994**, *116*, 405–413. [CrossRef]
63. *Reglamento de Instalaciones Térmicas En Los Edificios (RITE)*; Ministerio de la Presidencia: Madrid, Spain, 2007.
64. *ANSYS Ansys® Fluent 2020, Release 1, Help System, Theory Guide*; ANSYS, Inc.: Pittsburgh, PA, USA, 2020.
65. RESPILON Group, s.r.o. *Respilon Technical Data Sheet, Anti-Smog Window Membrane RWM*; RESPILON Group s.r.o: Brno, Czech Republic, 2018.
66. Buchta, S.; Šmarda, M.; Holomek, M. *Test Report 39-11216/1—Nanofilter Respilon Air*; Hudcova: Brno, Czech Republic, 2017.
67. Panitz, T.; Wasan, D.T. Flow Attachment to Solid Surfaces: The Coanda Effect. *AIChE J.* **1972**, *18*, 51–57. [CrossRef]
68. Reba, I. Applications of the Coanda Effect. *Sci. Am.* **1966**, *214*, 84–92. [CrossRef]
69. Kottek, M.; Grieser, J.; Beck, C.; Rudolf, B.; Rubel, F. World Map of the Köppen-Geiger Climate Classification Updated. *Meteorol. Zeitschrift* **2006**, *15*, 259–263. [CrossRef]
70. Crawley, D.; Lawrie, L. Climate.Onebuilding.Org. Available online: https://climate.onebuilding.org/ (accessed on 1 February 2022).
71. American Society of Heating, Refrigerating and Air-Conditioning Engineers. *2001 ASHRAE Handbook: Fundamentals SI Edition*; ASHRAE: Atlanta, GA, USA, 2001; ISBN 9781883413880.
72. AmesWeb Thermal Expansion Coefficient of Aluminum. Available online: https://amesweb.info/Materials/Thermal_Expansion_Coefficient_of_Aluminum.aspx (accessed on 22 February 2022).
73. Engineering ToolBox Metals—Temperature Expansion Coefficients. Available online: https://www.engineeringtoolbox.com/thermal-expansion-metals-d_859.html (accessed on 22 February 2022).
74. Pardal March, C.; Paricio Ansuategui, I.; Aguilar Urquidez, P.; Lopez Besora, J.; Flores Lazo, J.; Roig Mayoral, O. Sistema de Depuración Fotocatalítica. Patent Number P202030141, 27 January 2022.
75. Pardal March, C.; López Besora, J.; Alonso Montolio, C.; Cuerva Contreras, E.; Guardo Zabaleta, A.; Flores Lazo, J. Dispositivo Para Depuración de Aire Con Lamas Con Propiedades Fotocatalíticas (Modelo de Utilidad). Patent Number ES1248829, 17 September 2020.